Science Advances
AAAS

advances.sciencemag.org/cgi/content/full/5/11/eaav2869/DC1

Supplementary Materials for

Photoferrotrophy, deposition of banded iron formations, and methane production in Archean oceans

Katharine J. Thompson, Paul A. Kenward, Kohen W. Bauer, Tyler Warchola, Tina Gauger, Raul Martinez, Rachel L. Simister, Céline C. Michiels, Marc Llirós, Christopher T. Reinhard, Andreas Kappler, Kurt O. Konhauser, Sean A. Crowe*

*Corresponding author. Email: sean.crowe@ubc.ca

Published 27 November 2019, *Sci. Adv.* **5**, eaav2869 (2019)
DOI: 10.1126/sciadv.aav2869

This PDF file includes:

Supplemental Materials

Supplementary Materials and Methods

Experimental and growth media

The basal media was prepared after Hegler *et. al.*, 2008 (*61*) and allocated into serum bottles (100mL media, 160mL total volume), with 0.3g L^{-1} NH_4Cl, 0.5g L^{-1} $MgSO_4 \cdot 7H_2O$, 0.1g L^{-1} $CaCl_2 \cdot 2H_2O$. After autoclaving, 22mmol L^{-1} bicarbonate, trace elements, mixed vitamin solution, selenate-tungstate and vitamin B12 were added and the pH was adjusted to 6.8-6.9 under an N_2:CO_2 atmosphere (80:20). KH_2PO_4, Fe(II), and silica were added in a range of concentrations depending on the specific experiment (see Table S1).

All experiments were initially conducted using the standard media with 10mM Fe(II) and 4.4mM KH_2PO_4. In subsequent experiments, the media composition was adjusted to test the impact of a range of concentrations of Fe(II), PO_4^{3-}, and Si (Table S1) on the percentage of cells that remain suspended as opposed to depositing. This same range of Fe(II), PO_4^{3-}, and Si concentrations was further used to test the surface charge of the Fe(III) oxyhydroxides precipitated under these conditions (Figure 2a – main text, fig. S5a). The range of Fe(II), PO_4^{3-}, and Si concentrations was used to create a range of P:Fe(III) and Si:Fe(III) ratios (Figure 2b – main text). Specifically, Si concentrations were chosen to reflect the likely Si concentrations of the Precambrian oceans based on Jones *et. al.*, 2015 (*15*).

Fe(II) oxidation and cell growth

To track the growth kinetics of *Chlorobium phaeoferrooxidans* strain KB01 and *Chlorobium ferrooxidans* strain KoFox, sub-samples were taken from the serum bottles at the time of inoculation and every day thereafter. The first of these sub-samples were analyzed for Fe(II) and Fe(III) concentrations using spectrophotometric analyses. Specifically, Fe(II) and Fe(III) concentrations were measured using the ferrozine method and samples were measured directly as well as after being fixed in 1N HCl – after Voillier *et. al.*, 2000 (*62*). Fe(II) and Fe(III) concentrations were further used to identify when all of the Fe(II) had been oxidized to Fe(III) oxyhydroxides and therefore the appropriate time to determine the percentage of cells that remained suspended. Additional sub-samples were taken from these same serum bottles to measure the pigment concentrations. Pigments were measured spectrophotometrically after 24 hour extractions of 1mL of pelleted cells in acetone:methanol (7:2 v/v) (*63*). Pigment concentrations were then used as a proxy for cell abundance for both strains. To further confirm the growth of the strains, sub-samples were taken from the serum bottles and cells were fixed in gluteraldehyde (final concentration of 0.1%). After the cells were fixed they were subsequently stained with SYBR green (0.25% final concentration) and directly counted in a 96 well plate using a Miltenyi Biotec MACSQuant, with a flow rate of medium. Pigment concentrations were also used to determine the fraction of cells that remained suspended. An example of a growth curve for strain KB01 is shown in fig. S2 where the decrease in Fe(II) concentrations and an increase in cell counts confirm the growth of the strain.

Determination of cellular association to Fe(III)

C. phaeoferrooxidans strain KB01, *C. ferrooxidans* strain KoFox, and *Synechococcus* sp. were grown to late log phase in standard growth media (fig. S2). The bottles were gently shaken by inversion to mix cells and Fe(III) oxyhydroxides and allowed to settle for 24 hours. Mixing was done to resuspend cells that had settled out of the water column as a result of Stokes settling without any association to Fe(III) oxyhydroxides, and to allow maximum potential exposure of cell surfaces to Fe(III) oxyhydroxide particles. Sub-samples for Fe(II)/Fe(III) and pigments were taken from the upper portion of the serum bottle, avoiding settled Fe(III) oxyhydroxides. A second set of sub-samples was taken from each bottle after the bottle had been well mixed. Fe(II)/Fe(III) and pigment concentrations were measured as described above. The fraction of cells associated with Fe(III) oxyhydroxides was calculated by dividing pigment concentrations, a proxy for cell density (6.3×10^{-10} pigment/cell/mL for *C. phaeoferrooxidans* and 5.8×10^{-10} pigment/cell/mL for *C. ferrooxidans*), from the water column by the fully mixed suspensions. These measurements were conducted in 5 replicates and across a range of conditions (Table S1) – see Figure 2a in main text and fig. S5a. Association between both organisms and Fe(III) oxyhydroxide particles was further assessed through electron microscopy (described above). Images of strain KB01 are shown in the main text (Figure 3a, b), while images of KoFox and more TEM images of KB01 are shown below (fig. S3).

Zeta potential

To assess the surface charge of Fe(III) oxyhydroxides and cells, we determined the zeta potential of both using a Particle Metrix: ZetaView®. To prepare the Fe(III) oxyhydroxides for zeta potential measurements, they were first concentrated through centrifugation at 14 g for 10 seconds. The supernatant was then discarded and the Fe(III) oxyhydroxides were sonicated for 1 minute to loosen any cells from the Fe(III) oxyhydroxide particles. The Fe(III) oxyhydroxides were subsequently rinsed once in sterile MQ water and concentrated again via centrifugation. This process was repeated three times to reduce the numbers of cells associated with the Fe(III) oxyhydroxides to low (<100 cells mL^{-1}, counted through flow cytometry as described above) numbers. We confirmed that such low cell numbers had no impact on the surface charge of the Fe(III) oxyhydroxide particles by determining the zeta potential of Fe(III) oxyhydroxides produced through abiotic Fe(II) oxidation in sterile 1.0mM Si growth media. The zeta potential of these Fe(III) oxyhydroxides was the same as those produced in our experiments (data not shown). Fe(III) oxyhydroxides that we precipitated abiotically in sterile MQ water and in 0.7M NaCl exhibited a positive surface charge, as generally observed (*31*). The surface charges of biotically precipitated Fe(III) oxyhydroxides under the range of media compositions tested (described above) are shown in Figure 2b of the main text.

To determine the surface charge of the photoferrotrophic strains *C. phaeoferrooxidans* strain KB01 and *C. ferrooxidans* strain KoFox, both strains were grown to late log phase in 400 µM Fe(II), 1.0 mM Si, 3 µM PO_4^- media. The bottles were shaken and allowed to settle for 24 hours until all the Fe(III) oxyhydroxides had reached the bottom serum bottle. Cells were then collected

from water column and suspensions of Fe(III) oxyhydroxides and cells after mixing. The samples from the water column were centrifuged (10000 g) for 7 minutes and washed three times (7 minutes centrifugation at 10000 g between washes) in either Fe free growth media or 0.1 N NaCl. Each sample was then diluted 1/10 with filter-sterilized dH_2O (to lower the conductivity of the sample to <2000 µS cm^{-1}) and measured in triplicate using a Particle Metrix: ZetaView®. The samples of mixed cell-Fe(III) oxyhydroxide suspensions were first treated with pH 7 dithionite to reduce the Fe(III) to Fe(II). Fe(II) and Fe(III) concentrations were measured (as described above) before and after the dithionite treatments and the subsequent rinses to confirm that any residual Fe had been effectively removed (<2.5 µM) (data not shown). Following dithionite treatment, the mixed suspensions were measured in the same manner as the water column samples. Zeta potentials for each strain are summarized in fig. S4, while the zeta potentials for cells and Fe(III) oxyhydroxides measured in growth media and used in DVLO modeling are in Table S2.

Surface contact angles

To calculate the interfacial forces between the *C. phaeoferrooxidans* strain KB01, *C. ferrooxidans* strain KoFox, and the Fe(III) oxyhydroxides formed as by-product of their growth, we measured static contact angles for strain KB01, strain KoFox, and Fe(III) oxyhydroxides precipitated abiotically from silica-rich media. These measurements were conducted following Korenevsky and Beveridge, 2007 (*64*) and Saini and Chan, 2013 (*36*) and the contact angle data are summarized in Table S2. To conduct these measurements, cells and Fe(III) oxyhydroxides were collected onto a 0.22 µm polycarbonate filter until there was a thick lawn of cells or Fe(III) oxyhydroxides coating the entire filter. The filters were subsequently dried for 45-60 minutes to remove excess liquid prior to measurement. Contact angle measurements were conducted using a contact angle goniometer with three liquids that have known surface tension properties: water, glycerol, and diiodomethane (Table S2). 1 µL of each liquid was placed on the sample, 30 images were taken over the course of one and a half minutes, and contact angles were measured and averaged from these 30 images. This process was repeated three times for each of the reference liquids.

Cell surface titrations

To determine the acid-base chemistry and interrogate cell-surface functional groups, both strains *C. phaeoferrooxidans* strain KB01 and *C. ferrooxidans* strain KoFox were grown in 1.0 mM silica-rich media as described above. The cells were then removed from the media and pelleted through centrifugation. To remove residual Fe(III) oxyhydroxides the pelleted cells were treated for 10 minutes with 10 mL of oxalate/oxalic acid (pH 3) and 1 mL of 100 mM Fe(II) for every 1 mL of cells (*65-67*). To remove residual Fe(II) the cells were rinsed with anoxic iron-free growth media (*61*). Finally, the cells were resuspended in 200 mL of that same anoxic iron-free media. Cell suspensions were acid/base titrated following the protocol detailed in Martinez *et. al.* 2003 (*68*). Cells were centrifuged four times for 8 minutes at 6200 x *g*. In between these centrifugations the cells were rinsed three times with degassed MQ water and once with sterile, degassed 0.1 M KNO_3. The final pellet was resuspended in 0.1 M KNO_3. Sub-samples of 1 mL from this cell suspension were then used for each acid-base titration. The pH of the 1 mL sub-

sample was lowered to 3.5 using 200 µL of a 0.2 M sterile HNO_3 stock. These sub-samples were then placed inside a Metrohm glass titration vessel and covered with a Metrohm lid that was fit with a pH electrode and N_2 gas line. The pH meter was calibrated at three points – 4, 7, and 10 – prior to each experiment and the system was allowed to reach equilibrium by maintaining a constant pH reading for at least 180 minutes. Titrant additions occurred at a rate of less than 0.1 mV/min based on the settings of the autotitrator, which is adjusted to maintain a fixed interval of 0.15 pH units. These titrations were conducted between the pH values of 3.5 and 11 and were subsequently modelled (*68-70*). Results from the cell surface titrations are shown in Table S2.

Electron microscopy (SEM, TEM)

Cells for SEM were grown up to late log-early stationary phase in regular growth media (10 mM Fe(II), 4.41 mM phosphate). The cell-Fe(III) oxyhydroxide suspensions were gently shaken and allowed to settle for 24 hours. A 1 mL sub-sample was collected from either the upper portion of the serum bottle, avoiding settled Fe(III) oxyhydroxides, or from the mixed suspension after gentle shaking. The samples were placed on a Nucleopore Track-Etched Membrane from Whatman®. The cells were then fixed with 2.5% gluteraldehyde buffered with 0.1 M PIPES at pH of 7.4. The external cellular structures were preserved using a 1% osmium tetroxide solution buffered with 0.1 M PIPES at pH 6.8. Filters were rinsed gently with MQ water and then dried using an ethanol dehydration series. The filters were critical-point-dried using a Samdri795 from Toosimis Research Corporation. Finally, the filters were attached to a stub and coated with 5nm of iridium to ensure conductivity. The filters were imaged on a Helios SEM. Fe(III) oxyhydroxides and cells were confirmed through energy-dispersive X-ray spectroscopy (EDS) measurements of carbon and iron abundances and multiple points were measured for each surface found. SEM images are shown in Figure 3 of the main text and fig. S3. Cells for TEM were concentrated through centrifugation. The cells were then frozen rapidly using a LEICA EM HPM100. The cellular water was replaced with an alcohol mix while in liquid nitrogen; the samples were sliced as thin sections from an epoxy block and placed onto a copper grid. The samples were imaged on an Osiris S/TEM at the 4D labs imaging facility at Simon Fraser University. TEM images are shown in Figure 3 of the main text and fig. S3.

Particle size

To assess the particle-size distribution of Fe(III) oxyhydroxides formed during photoferrotrophy, Fe(III) oxyhydroxides produced by strains KB01 and KoFox in standard media containing 3 µM PO_4^{3-} and 1.0 mM Si were concentrated and rinsed as described for zeta potential measurements above, and particle sizes determined using a Mastersizer2000. To reduce artificial clumping during measurement, the Fe(III) oxyhydroxide particles were sonicated for 1 minute in the Mastersizer2000 prior to their measurement. The particles were then stirred continuously during measurement to reduce aggregation. The particle size distribution data are shown in fig. S6.

Supplementary Text

Section S1. Cell surface features and acid-base chemistry

To quantify the observed differences between strain KB01 and strain KoFox we determined the acid-base chemistry of the cell surfaces of both strains using titrations, as described above. Results of these experiments (Table S2) indicate a clear difference between the surface functional groups of these organisms with strain KB01 having proportionally more amine groups than carboxyl. The surface of strain KoFox, conversely, is dominated by carboxyl functional groups, which are present at much higher density on the surface of strain KoFox than KB01 and have different *p*Ka values, notably the functional group on KoFox with *p*Ka of 4.05 ± 0.12 (Table S2). These additional surface functional groups on strain KoFox cells have strong potential to bind metals like Fe(III), which by binding with anionic surface species would offset the overall negative surface charge. To test the possible role of Fe(III) in reducing surface charge on strain KoFox, we treated cells with dithionite to reduce surface bound Fe(III) to Fe(II) and liberate it from cell surfaces. Dithionite treated KoFox cells became more negatively charged, as expected. Dithionite treatments had correspondingly little effect on the surface charge of strain KB01 cells indicating a lack of Fe(III) binding to KB01 cell surfaces. The presence of functional groups that bind Fe(III) on strain KoFox surfaces thus appears to explain the different charges on the two strains. Notably, benthic microorganisms often develop surface layers rich in such anionic functional groups to facilitate particle adherence. We explore this in more detail below.

Detailed electron microscopy revealed that strain KB01 cells were almost exclusively free of Fe(III) oxyhydroxides and characterized by a surface texture that was free of any obvious extracellular features (Figure 3a, b – main text; fig. S3 g, h). While cells of strain KoFox clearly avoided encrustation by Fe oxyhydroxides, they were almost invariably associated with Fe(III) oxyhydroxide particles and situated in multicellular aggregates with Fe(III) oxyhydroxides (fig. S3 a, b, c, e, f). Unlike the rather featureless surfaces of strain KB01 cells, KoFox cell surfaces are characterized by long (20-100 nm), thin (<5 nm) tendrils (fig. S3 d, e, f), which can be observed under iron-free (fig. S3d) and iron-rich conditions (fig. S3 e, f). Furthermore, under iron-rich conditions tendrils appear to be directly associated with Fe(III) oxyhydroxides (fig. S3 e, f). These tendrils are reminiscent of bacterial capsules observed on other organisms including *Escherichia coli* K30, *Pseudomonas aeruginosa* FRD1, and *Shewanella oneidensis* (*37, 71*). Bacterial capsules are commonly excreted by benthic microorganisms as a mode of cellular defense, and to adhere to mineral surfaces or bind particles (*37, 71*). Such capsules are commonly comprised of EPS and are thus rich in carboxyl surface groups as we observed for strain KoFox. We thus attribute the difference in surface properties between strains KB01 and KoFox to the excretion of this capsule-like surface coating by the latter. Such a capsule-like extracellular feature likely sets benthic photoferrotrophic Chlorobi apart from their pelagic counterparts given the obvious advantages of capsule formation to a benthic lifestyle and the challenges it would present to a pelagic lifestyle.

Section S2. Cell-iron surface interaction and extended DVLO modeling

To assess the biophysical controls on the association between Fe(III) oxyhydroxides and cell surfaces, we conducted Derjaguin, Landau, Verwey and Overbeek (DVLO) and extended DVLO modeling (*36, 38, 64, 72*). DVLO modeling allows us to describe both short range interactions, such as Lewis acid-base forces, as well as long range interactions, such as electrostatic forces, which combine to control the association between bacterial cell surfaces and Fe(III) oxyhydroxides. To determine the individual forces and thus the sum force (total) or interaction energy between cell surfaces and Fe(III) oxyhydroxides, we calculate the surface tension properties for the cell surfaces and Fe(III) oxyhydroxides as

$$\gamma^{TOT} = \gamma^{LW} + \gamma^{AB} \quad (1)$$

where γ represents surface tension (in mJ m^{-2}) and TOT is the total surface tension, LW is the apolar Lifshitz-van der Waals surface tension, and AB is the polar Lewis acid-base surface tension. The AB component of equation 1 can be further broken down into electron donating (γ^-) and electron accepting (γ^+) components

$$\gamma^{AB} = 2\sqrt{\gamma^+\gamma^-} \quad (2)$$

These values can be determined for a given surface (*S*) through measurements of surface contact angles (θ) between the solid and three liquids (*L*) with known surface tensions (Table S2). Using these contact angles, Young's equation can be solved for the unknown surface tension (*S*) of the cells and Fe(III) oxyhydroxides (*38, 72*).

$$(1 + cos\theta) * \gamma^{TOT} = 2\left(\sqrt{\gamma_S^{LW}\gamma_L^{LW}} + \sqrt{\gamma_S^+\gamma_L^-} + \sqrt{\gamma_S^-\gamma_L^+}\right) \quad (3)$$

The calculated surface properties for *Chlorobium phaeoferrooxidans* strain KB01, *Chlorobium ferrooxidans* strain KoFox, and abiotically precipitated iron oxyhydroxides are shown in Table S2. These surface properties can then be used to calculate the Gibbs free energy for an interaction between two identical particles '*i*' in water '*w*' (ΔG_{iwi}) [Eq.4] and two different particles '*i*' and '*j*' in water '*w*' (ΔG_{iwj}) [Eq.5]

$$\Delta G_{iwi} = \Delta G_{iwi}^{AB} + \Delta G_{iwi}^{LW} = -2 * \left(\sqrt{\gamma_i^{LW}} - \sqrt{\gamma_w^{LW}}\right)^2 - 4 * \left(\sqrt{\gamma_i^+\gamma_i^-} + \sqrt{\gamma_w^+\gamma_w^-} - \sqrt{\gamma_i^+\gamma_w^-} - \sqrt{\gamma_w^+\gamma_i^-}\right) \quad (4)$$

and

$$\Delta G_{iwj} = \Delta G_{iwj}^{AB} + \Delta G_{iwj}^{LW} = 2\left[\sqrt{\gamma_i^{LW}\gamma_w^{LW}} + \sqrt{\gamma_j^{LW}\gamma_w^{LW}} - \sqrt{\gamma_i^{LW}\gamma_j^{LW}} - \gamma_w^{LW} + \sqrt{\gamma_w^+}\left(\sqrt{\gamma_i^-} + \sqrt{\gamma_j^-} - \sqrt{\gamma_w^-}\right) + \sqrt{\gamma_w^-}\left(\sqrt{\gamma_i^+} + \sqrt{\gamma_j^+} - \sqrt{\gamma_w^+}\right) - \sqrt{\gamma_i^+\gamma_j^-} - \sqrt{\gamma_j^+\gamma_i^-}\right] \quad (5)$$

Here, a positive ΔG indicates a thermodynamically unfavorable interaction (repulsion) between the two particles, while a negative ΔG indicates a thermodynamically favorable interaction (attraction).

Using this modeling approach, both strain KB01 and strain KoFox had low electron-accepting (<2.2 mJ m^{-2}) and high electron donating (>44 mJ m^{-2}) attributes, which is consistent with surface tensions reported for other bacterial strains such as *S. putrefaciens* (*64*) and *M. ferrooxydans* strain PV-1 (*36*). These properties suggest that the cell surfaces of both strain KB01 and strain KoFox are monopolar and hydrophilic (*38*). Furthermore, when the free energy of interaction was calculated for both strains, strain KB01 and strain KoFox had large positive ΔG_{iwj}^{AB} (Table S2) conferring a large repulsive force that overwhelmed a much smaller attraction arising from Lifshitz-van der Waals forces, resulting in a positive overall ΔG_{iwj} of 33.3 mJ m^{-2} and 24.1 mJ m^{-2} respectively, and net repulsion (Table S2). The total interaction energy between two surfaces, however, also includes an electrostatic force and the combination of all 3 forces can vary depending on the distance between two surfaces. Extended DVLO modeling can be used to determine how these forces vary with distance and thus assess net attraction or repulsion.

Extended DVLO modeling determines the contribution of each individual force – Lewis acid-base (AB), Lifshitz-van der Waals (LW), and electrostatic (EL) – over a specified distance between surfaces by summing the three individual interaction energies

$$\Delta G^{TOT} = \Delta G^{AB} + \Delta G^{LW} + \Delta G^{EL} \quad (6)$$

To calculate each of these individual ΔG's, an assumption has to be made regarding the geometry between the interacting cell surface and the iron particle. For all calculations we assumed, therefore, that the cell surface was equivalent to a semi-infinite plate, and the diameter of the Fe(III) oxyhydroxide particle was 1 nm (Figure 2c – main text; fig. S5c) or 10 nm (data not shown). Additionally, all free energies are calculated as a function of the distance between the cell surface and the iron oxyhydroxide particle over a distance of 5nm. Using the assumed geometry and distances, the Lewis acid-base (ΔG^{AB}) interaction energy equation is

$$\Delta G^{AB}(d) = 2\pi r\lambda * \Delta G_{iwj}^{AB} * e^{\frac{[d_0 - d]}{\lambda}} \quad (7)$$

where r is the radius of the iron oxyhydroxide particle, λ is the correlation length of the molecules in the liquid medium (~0.6 nm), d is the separation distance, d_o is the distance of closest approach between the cell surface and the Fe(III) oxyhydroxide particle (0.157 nm) (*38*) and ΔG_{iwj}^{AB} is the AB component of the cell-Fe(III) oxyhydroxide free energy of interaction (Table S2).

The Lifshitz-van der Waals interaction energy (ΔG^{LW}) equation is

$$\Delta G^{LW}(d) = -\frac{A}{6}\left[\frac{2r(d+r)}{d(d+2r)} - \ln\left(\frac{d+2r}{d}\right)\right] \quad (8)$$

where *r* is the radius of the Fe(III) oxyhydroxide particle, *d* is the separation distance, *A* is the Hamakar constant. The Hamakar constant between two identical particles is given as

$$A_{ii} = 24\pi b_0^2 \gamma_i^{LW} \quad (9)$$

where d_0 is the minimum separation distance between two semi-infinite planar surfaces in van der Waals contact (average of 0.157 nm) (*73*) and γ_i^{LW} represents the LW surface tension component of the particle in question (Table S2). The Hamakar constant can then be calculated separately for each photoferrotrophic strain by calculating the individual Hamakar constants for the bacteria '*b*' and the Fe(III) oxyhydroxide surface '*s*' in water '*w*' through the following equation

$$A_{bws} = \left(\sqrt{A_{bb}} - \sqrt{A_{ww}}\right) * \left(\sqrt{A_{ss}} - \sqrt{A_{ww}}\right) \quad (10)$$

Finally, the electrostatic interaction as a function of the separation distance between the cell surface and the Fe(III) oxyhydroxide particle can be calculated as follows

$$\Delta G^{EL}(d) = \pi\varepsilon\varepsilon_0 r(\phi_b^2 + \phi_s^2) * \left\{\frac{2\phi_b\phi_s}{\phi_b^2+\phi_s^2} * \ln\left[\frac{1+e^{(-\kappa d)}}{1-e^{(-\kappa d)}}\right] + \ln\left[1 - e^{(-2\kappa d)}\right]\right\} \quad (11)$$

where ε is the dielectric constant of the interacting medium (80), ε_0 is the permittivity of a vacuum (8.854 x 10^{-12} C^2 J^{-1} m^{-1}), *r* is the radius of the Fe(III) oxyhydroxide particle, ϕ_b and ϕ_s are the zeta potentials of the bacteria and Fe(III) oxyhydroxide respectively (in JC^{-1}; Table S2 – reported in mV, conversion factor of 10^{-3}), *d* is the separation distance, and κ is the reciprocal Debye length (*74*). The reciprocal Debye length can be calculated as follows

$$\kappa = \sqrt{\frac{2000 * N_a * I * e^2 * Z^2}{\varepsilon * \varepsilon_0 * \varkappa * T}} \quad (12)$$

where N_a is Avogadro's number (6.022 x 10^{23}), I is the ionic strength of the medium (0.001 M in our experiments), e is the elementary charge (1.6 x 10^{-19} C), Z is the valence of the electrolyte medium (2), $\varkappa$ is Boltzmann's constant (1.38 x 10^{-23} m^2 Kg s^{-2} K^{-1}), and T is temperature (K) (*38*, *75*).

Results for the extended DVLO modelling indicate that both strain KB01 and strain KoFox have positive primary maxima (20 kT and 15 kT respectively) that are dominated by a strong Lewis acid-base repulsion (Figure 2c – main text, fig. S5 c). At a distance of 3 nm, however, the electrostatic interaction force becomes the dominant force under all conditions. In the case of strain KB01, the electrostatic force maintains a strong positive interaction energy (repulsion between cell surface and Fe(III) oxyhydroxide), which results a consistently positive overall interaction energy with no negative minimum for strain KB01 (Figure 2c – main text). This result corroborates the results of the cell separation experiments, described above and shown in Figure 2a, b in the main text, demonstrating that a repulsive electrostatic force maintains the separation between the cell surface of strain KB01 and the negatively charged Fe(III) oxyhydroxides. When the charge of the Fe(III) oxyhydroxides is positive, however, the extended DVLO modelling

generates a negative minimum at approximately 3nm that continues over the remaining distance (data not shown), which suggests a weak attraction between strain KB01 and the Fe(III) oxyhydroxides and explains the much higher numbers (50%) of strain KB01 cells seen in the sediments when the strain is grown in medium with low P and Si concentrations that leads to positively charged Fe(III) oxyhydroxides (Figure 2a – main text). The AB interaction force, for strain KoFox, leads to a primary positive maximum, which is similar albeit a bit lower in magnitude than that of strain KB01. Regardless of whether the Fe(III) oxyhydroxides are negative (fig. S5c) or positive (data not shown), however, the electrostatic interaction energy creates a weakly negative minimum between 4 and 4.5nm (fig. S5c). This weak attractive interaction force supports the results of the cell separation experiment (Figure 2a – main text, fig. S5a) and the association between strain KoFox cells and Fe(III) oxyhydroxides seen in the SEM and TEM images of strain KoFox (fig. S3). The extended DVLO modelling demonstrates that both forces that arise from acid-base and electrostatic interactions lead to repulsion between strain KB01 and Fe(III) oxyhydroxides, allowing this pelagic photoferrotroph to physically separate itself from its growth byproduct and thus remain suspended. DVLO modeling thus reveals differences between *Chlorobium phaeoferrooxidans* strain KB01, which does not interact with Fe(III) oxyhydroxides and *Chlorobium ferrooxidans* strain KoFox, which forms a weak association with Fe(III) oxyhydroxides. The association between KoFox and Fe(III) oxyhydroxides is, however, weak and only appears at a distance of 3nm or more between surfaces.

Section S3. Iron concentration and supply

To address an apparent deficiency in global Fe(II) fluxes to the oceans required to sustain BIF deposition during the Archean Eon, we re-evaluated both modern and Precambrian global Fe budgets with new information on material and energy fluxes for modern and Precambrian hydrothermal and weathering systems. Previous estimates for Fe(II) fluxes in the modern oceans are based on the product of hydrothermal fluid fluxes of 3×10^{13} kg $yr^{-1} \pm 1.5 \times 10^{13}$ kg yr^{-1} (*41*) and Fe(II) concentrations measured in these fluids, ~6 mmol kg^{-1} (*41*), which yield a global flux of Fe(II) from hydrothermal vents of 0.3 ± 0.1 Tmol yr^{-1} (*76*). Fe(II) is also delivered to modern oceans through extensive, yet poorly quantified, low temperature off-axis hydrothermal venting (*41*), where measurements of fluid flow (2.5×10^{15} kg yr^{-1} (*41*)) and Fe(II) concentrations (~0.75 mmol kg^{-1} (*41*)) suggest these systems contribute 6 times more Fe(II) to the global oceans, at rates of 1.88 Tmol yr^{-1}. Combining on- and off-axis estimates yields a total Fe(II) hydrothermal flux of ~2 Tmol Fe yr^{-1} to the modern oceans and this is insufficient to sustain BIF deposition (Table 3, part 1). These previous estimates of Fe(II) fluxes to the modern oceans, however, may still underestimate total hydrothermal leaching of Fe(II) from ocean crust due, in-part, to the poorly quantified off-axis hydrothermal circulation. We thus re-estimated the modern hydrothermal Fe leaching with new fluid flow estimates from a recent compilation, as described in the main text (*47*). While the on-axis Fe concentration remains unchanged, the off-axis hydrothermal Fe leaching increases to 10.5 Tmol Fe yr^{-1} (Table S3, part 2). Combining on and off-axis fluxes gives a new upper estimate on modern hydrothermal Fe leaching of ~11 Tmol yr^{-1}, and while we use this value as a point of departure for reconstructing Fe fluxes in the Precambrian Eons, it should be further tested through direct measurements in the modern.

Including the new estimates of off-axis hydrothermal Fe(II) flux increases the overall Fe(II) flux to the global oceans to values that could sustain BIF deposition without depleting the oceans of Fe(II) for hundreds of millions of years.

Given that global Fe fluxes would have been much different in the Archean Eon due to conditions that differ from the modern, such as pervasively anoxic oceans, reduced seawater sulfate (*42*, *44*), and enhanced hydrothermal activity (*40*, *42*), we sought to further reconcile the global Fe budget during the Archean Eon. To account for the enhanced Archean hydrothermal fluid flow, we scaled modern fluid flow by the ratio of past to modern lithospheric heat loss. We calculated the global lithospheric heat loss (Q) for any age lithosphere (t), at geologic time (τ), using the following equation

$$Q(t,\tau) = 2\left(\frac{2A}{t_m}\right)(t_m)^{\frac{1}{2}}\left[\left(\frac{t}{t_m}\right)^{\frac{1}{2}} - \left(\frac{1}{3}\right)\left(\frac{t}{t_m}\right)^{\frac{3}{2}}\right] \quad (13)$$

where

$$t_m = 180 - 38.2\tau \quad (14)$$

t is 1 m.y., and A is a calculated ratio for continental growth. We utilized a linear continental growth model (*77, 78*) and calculated A as follows

$$A = \frac{C_m}{(-0.1\tau+1)} \quad (15)$$

where C_m is the size of the modern continents as a fraction of the Earth's surface size, and τ is the geologic time. To calculate the heat loss ratio for each geologic time, we normalized each calculated Q to the Q value calculated for the modern (Table S3). Finally, we used this ratio to scale hydrothermal fluid flow, calculating past on- and off-axis hydrothermal fluid flow for the Proterozoic and Archean Eons as seen in the main text and in Table S3.

To assess the delivery flux of Fe(II) to Archean oceans from continental weathering we scaled the modern rate of Fe delivery to the Archean. Reactive Fe is delivered to the modern oceans as Fe(III) (oxyhydr)oxides at a rate of 6.5 ± 1.7 Tmol yr^{-1}, as mineral bound Fe(II) is oxidized during weathering under the well oxygenated modern atmosphere. Under the low oxygen Archean atmosphere, a fraction of the reactive Fe would have been weathered as Fe(II). While the concentration of Fe(II) in the Precambrian crust was likely higher than it is in the modern (*79*), which would result in a larger flux of Fe(II) to the oceans, the total continental area was smaller. To estimate the weathering flux of Fe(II) to the oceans in the Archean Eon, we used an estimate for Mg^{2+} (*15*) weathering fluxes (5.5 Tmol yr^{-1}) and multiplied these by the ratio of Mg to Fe in the Precambrian crust (1.2) (*79*), for an Fe(II) flux of 6.6 Tmol y^{-1}. Recognizing that weathering rates are proportional to continental area, we scaled this number by 0.75 to account for smaller continents at 2.5 Ga although this value may have been as much as a factor of two smaller during the early Archean (*43*), resulting in an Fe(II) weathering flux of 5 Tmol yr^{-1} to the oceans.

Section S4. Physical separation of ferric iron oxyhydroxides and cellular biomass in an ocean setting

To evaluate the impact of the physical separation of pelagic photoferrotrophs from their Fe(III) oxyhydroxide byproducts in an ocean upwelling setting we created a model detailing the impact of horizontal ocean current velocities on the deposition of Fe(III) oxyhydroxides and cellular biomass to the seafloor. To calculate the distance that an Fe(III) oxyhydroxide particle or cell travels prior to deposition, we first calculated the settling velocity for the Fe(III) oxyhydroxide particles and cells. Settling velocity was calculated according to Stokes law

$$S_v = \frac{(P_p - P_w) * g * d^2}{18\eta} \quad (16)$$

where P_p is the density of the particle (Fe(III) oxyhydroxide or cell), P_w is the density of seawater at 20°C (1.025 g cm^{-3}), g is gravitational acceleration (9.8 m s^{-2}), d is the diameter of the particle (Fe(III) oxyhydroxide or cell), and η is the dynamic viscosity of seawater at 20°C (0.00108 kg m^{-1} s^{-1}). For this model, the density of ferrihydrite (3.8 g cm^{-1}) was used to simulate biogenic Fe(III) oxyhydroxides (*5*, *23*), while the density of an *E. coli* cell (average of 1.08 g cm^{-1}) was taken from the literature (*80*). To represent a realistic range of Fe(III) oxyhydroxide particle diameters, particle sizes were measured (as described above) and the measured sizes fit with a lognormal probability distribution according to

$$p(x) = \frac{e^{\frac{-(\ln(x)-\mu)^2}{2\sigma^2}}}{\sigma * \sqrt{2\pi} * x} \quad (17)$$

where the value of μ is 1.9 and the value of σ is 1.1 based on the data. We then applied a simple aggregation factor to the lognormal distribution where the smallest particle (0.01 µm) grew to be twice its size, and particles greater than 28.6µm remained the same size, and the growth rate of all particles in between was scaled linearly (*81*) (fig. S6). The diameters of strain KB01 and strain KoFox range from 250 nm to 1 µm with a median of 500 nm. The distribution of cell sizes was also modelled using a lognormal probability distribution (equation 17; μ is 0.5 and σ is 1.012) based on cell imaging (data not shown). The particle sizes for both the Fe(III) oxyhydroxides and cells were then used to calculate the Stokes settling velocity for each individual particle. We then calculated the distance that each particle would travel given a 150 meter deep water column (typical depth of a coastal shelf) using horizontal water velocities typical for coastal margin settings (*52*, *55*). Results of this model illustrate the effective physical separation of the Fe(III) oxyhydroxides and cellular biomass produced in upwelling provinces under all reasonable conditions (fig. S6 and Table S4). Furthermore, the cellular biomass travels distances that are similar to the width of modern oceans, indicating that the biomass produced through photoferrotrophy in an upwelling province would have been dispersed throughout all oceanic provinces.

Section S5. Box model of Archean marine carbon and iron cycles

To evaluate the global rates of photoferrotrophy, iron oxyhydroxide deposition, and methane production we constructed an oceanic box model. To create the box model, we split the upper ocean into the three oceanic provinces (*52*) – upwelling, coastal, and open-ocean – and subsequently added the pertinent carbon and iron fluxes as the inputs and outputs of each box (Figure 4b, main text). We treated the upper ocean of each province separately and calculated primary production for each of these provinces as

$$PP_p = [Fe(II)]_D * A_p \quad (18)$$

where A_p is the upwelling rate (m y^{-1}) in the oceanic province of interest, $[Fe(II)]_D$ is the deep ocean Fe(II) concentration, and PP_p is the primary production specific to that province. We tested a range of deep ocean Fe(II) concentrations (0-100 μM; Figure 5c – main text) and upwelling rates specific to each province as guided by relevant values from the modern ocean (0-1500 m y^{-1} – upwelling province; Figure 5d – main text, 0-100 m y^{-1} – coastal province; fig. S8a, 0-5 m y^{-1} – open ocean; fig. S8b) (*52, 55*). Once the primary production (in mol m^{-2} y^{-1}) for each province has been calculated, global primary production was calculated by multiplying each province by its areal extent

$$PP_G = \left[\left(\frac{S_{Up}}{S_G}\right) * PP_{Up}\right] + \left[\left(\frac{S_{Cp}}{S_G}\right) * PP_{Cp}\right] + \left[\left(\frac{S_{Op}}{S_G}\right) * PP_{Op}\right] \quad (19)$$

where S_{Up}, S_{Cp}, and S_{Op} are the areal extents of the upwelling, coastal, and open ocean provinces respectively (m^2), and S_G is the area of the whole ocean (m^2). We tested the effect of continental growth (0-100% of modern continental size; Figure 5a – main text) by reducing the area of the ocean in response to increasing continental areas while maintaining a fixed ratio of upwelling and coastal province area to continental area (i.e. with larger continents come larger upwelling and coastal provinces). Thus, changing the size of the continents changes the contribution that each province makes to total ocean area and global primary production (Figure 5a – main text). Rates of other biogeochemical processes were calculated in a similar fashion by replacing the *PP* in equation 19 with the biogeochemical process of interest.

Organic carbon produced during primary production was distributed into two pools: 1) Fe(III) oxyhydroxide associated biomass, and 2) free, unassociated biomass. Fe(III) associated biomass settled and was deposited within the oceanic province in which it was produced, whereas given the broad dispersal of cellular material, the unassociated biomass was evenly distributed across the global ocean. Settling rates of Fe(III) oxyhydroxides are sufficiently rapid that we ignored degradation of biomass associated with Fe(III) oxyhydroxides in the water column. Settling of unassociated biomass is much slower and is thus subject to degradation within the water column. To calculate the organic carbon that is degraded through iron reduction and methanogenesis as it sinks to the ocean floor, we used a power law (*52*)

$$F = F_{100} * \left(\frac{z}{100}\right)^{b} \quad (20)$$

where F is the amount of organic carbon degraded (in mol m^{-2} y^{-1}), z is the depth of the oceanic province, the exponent, b, is the log-log slope scaled for anaerobic respiration (0.36 (*53*)), and F_{100} is the log-log of the carbon degradation rate data (*52*). F_{100} is dependent on the rate of primary production and is calculated, therefore, using the relationship between F_{100} and the primary production in a given province (*52*)

$$F_{100} = 0.0677 * (PP_G)^{1.3041} \quad (21)$$

where PP_G is global primary production (as calculated above). Finally, we calculated the final value for F by integrating the values for F over two different depth intervals – 150 m for the upwelling and coastal provinces and 3000 m for the open ocean – using 12.5 m intervals for z. Given that iron reduction is generally thermodynamically more favorable than methanogenesis (*82*), we channeled biomass degradation first through Fe-reduction until Fe(III) oxyhydroxides were entirely reduced and then through methanogenesis, once Fe(III) oxyhydroxides were exhausted. Rates of degradation were calculated for individual provinces and global rates calculated by summing the 3 provinces (Equation 19). Residual organic carbon and Fe(III) oxyhydroxides – if not quantitatively degraded in the water column – were deposited in the sediments of each province. The organic carbon that reaches the sediments is the sum of Fe(III) oxyhydroxide associated carbon for that province and residual mean global unassociated carbon that escaped degradation in the water column. We, thus, calculated the organic carbon that reaches the sediments in a specific province using the following equation

$$C_s = \{[PP_G * (1 - A)] - WC_d\} + \left(PP_p * A\right) \quad (22)$$

where C_s (in mol m^{-2} y^{-1}) is the biomass carbon that reaches the sediments, PP_G is the global primary production, A is the fraction of cells that are associated with Fe(III) oxyhydroxides, WC_d is the amount of carbon degraded in the water column of that province, and PP_p is the primary production of the specific province. Furthermore, given the strain dependent differences in cell-Fe(III) oxyhydroxide association discussed in the main text (Figure 2a – main text, fig. S5a), we used equation 22 to test the impact of cell-Fe(III) oxyhydroxide associations (between 0-100%: Figure 5b – main text) on the outputs of the model.

The flux of biomass carbon that reaches the sediments in each of the three provinces was calculated with Equation 22 but some of this carbon is subject to degradation during diagenesis. We estimated that the fraction of carbon buried is 15% of that deposited, based on carbon burial in modern ferruginous lakes (*56, 83, 84*). We further tested the impact of this burial efficiency by changing efficiency from 0-50% (fig. S8c). The biomass carbon not buried was again used to fuel Fe(III) reduction and methanogenesis in that order. If the biomass carbon delivered to the sediment (less carbon buried) exceeded Fe(III) supply, then the remaining biomass carbon was channeled through methanogenesis. Given that the greatest area specific rates of primary production, and therefore Fe(III) oxyhydroxide formation, occurred in the upwelling province,

and that much of the corresponding biomass was exported to other provinces, all biomass carbon deposited in sediments underlying the upwelling province was channeled through Fe(III) reduction. Methanogenesis, on the other hand, occurred when all the Fe(III) oxyhydroxides were consumed in the coastal and open ocean provinces. Given the formation of Fe(III) oxyhydroxides in each province, we calculated the rate of Fe(III) oxyhydroxide deposition (in mol m^{-2} y^{-1}) through the following equation

$$Fe(III)_p = \left(PP_p * 4\right) - (WC_{dFe} * 4) - (S_{dFe} * 4 * R_{IR}) \quad (23)$$

where the water column carbon degradation channeled through iron reduction (WC_{dFe}), multiplied by the 4:1 Fe:C ratio of photoferrotrophy, and the sediment carbon degradation channeled through iron reduction (S_{dFe}) (multiplied by the 4:1 ratio) are subtracted from the total primary production in a given province (PP_p) (multiplied by the 4:1 ratio). R_{IR} is the fraction of the Fe(III) oxyhydroxide Fe that is reduced in the sediments and re-enters the water column by diffusion as dissolved Fe(II). We used a fraction of 0.25, constrained by the rates of recycling observed in modern Archean ocean analogues (*85*), and then further tested the impact of Fe(III) oxyhydroxide recycling on the model output by running fractions between 0 and 0.5 (fig. S8d).

Finally, to calculate global rates of Fe(III) reduction and methanogenesis, we tallied the water column and sediment rates and multiplied them by the size of the global ocean (in m^2) to calculate the global rate in Tmol yr^{-1} (Table 1 – main text). Global rates of total Fe(III) oxyhydroxide production, Fe(III) deposition, Fe recycling, and primary production were calculated in Tmol yr^{-1} (Table 1 – main text). Overall the model illustrates the magnitude of the coupled Fe and carbon biogeochemical cycles that could have been supported by an Archean Earth system in which primary production is driven by photoferrotrophy.

Section S6. Organic carbon burial and diagenesis

Siderite is an important component of BIF, and at least some of the siderite in BIF is diagenetic. For example, carbon isotopes can be used to estimate the amount of diagenetic siderite in BIF. The isotopic composition of carbon in BIF siderite varies from -5 ‰ to -10 ‰ across different units with an approximate average of -7 ‰ (*24, 86*), while the carbon isotopic composition of seawater is estimated at 0 ‰ and the isotopic composition of organic carbon is estimated at -30‰. Assuming that carbon in siderite is a mixture of carbon from seawater carbonate and carbonate produced during diagenetic respiration of organic matter, the fraction of diagenetic carbon in siderite can be estimated through isotopic mass balance. Based on the values above then, we estimate 30% of the carbon in BIF siderite is diagenetic.

This example places constraints on the amount of organic carbon that needs to be deposited in BIF in order to support diagenetic siderite. Again, for example, assuming our benchmark model parameters with 15% cell-Fe(III) association – 1.2 mol C m^{-2} yr^{-1} reaches sediments underlying the upwelling province. 15% of which is considered unreactive and is buried, leaving a reactive carbon flux of 1 mol C m^{-2} yr^{-1} to support siderite formation. In the benchmark scenario, 30.8 mol Fe m^{-2} yr^{-1} Fe(III) deposited and the 1 mol C m^{-2} yr^{-1} supports the reduction of 4 mol Fe m^{-2} yr^{-1},

leaving 27 mol Fe(III) m^{-2} yr^{-1}. 25% of the Fe(II) produced through reduction is recycled into the water column, leaving 3 mol Fe m^{-2} yr^{-1} to form diagenetic siderite. Assuming that 30% of the siderite is diagenetic based on carbon isotopes (see above) this leads to 10 mol Fe(II) m^{-2} yr^{-1} siderite deposition. In this example then, BIFs contain 27% iron as siderite and the remainder as ferric iron phases, which results in a mean redox state of 2.7. This redox state is similar to many units found in Neoarchean BIFs (fig. S1, Table S5).

Finally, to compare carbon deposition rates from our model with the geologic record we estimated the fractional contribution of organic carbon to total sedimentation rates by assuming total sedimentation rates similar to those determined for a range of modern environments (fig. S7). The resulting organic carbon concentrations at the lower sedimentation rates characteristic of modern deep water environments are similar to those found in organic carbon-rich Precambrian shales (fig. S7; Figure 1 – main text; Table S5), while higher sedimentation rates lead to organic carbon contents similar to typical coastal margin sediments.

Supplementary tables

Table S1. Range of concentrations in the growth media used throughout experiments.

	$FeCl_2$	**Silica**	**KH_2PO_4**
Standard growth media	10 mM	0 mM	4.4 mM
Low P	250 µM-500 µM	0 mM	3-6 µM
Low P, low Si	250 µM-500 µM	0.6 mM	3-6 µM
Low P, middle Si	250 µM-500 µM	1.0 mM	3-6 µM
Low P, high Si	250 µM-500 µM	1.5 mM	3-6 µM

Table S2. Cell surface characteristics and cell-mineral interaction modeling.

Part 1: Summary of pKa and site concentration values from Langmuir isotherm/LPM optimization

Site	****pK_a**	****Site concentration (mol/g) x 10^{-4}**	**Suggested functional group assignment***
Strain **KB01** - 1	6.14 ± 0.26	2.63 ± 0.26	Carboxyl or phosphoryl
Strain **KB01** - 2	7.27 ± 0.17	2.21 ± 0.04	Amine
Strain **KB01** - 3	8.70 ± 0.37	1.76 ± 0.41	Amine
Strain **KoFox** - 1	4.05 ± 0.12	4.25 ± 0.08	Carboxyl or phosphoryl
Strain **KoFox** - 2	6.55 ± 0.23	25.1 ± 0.28	Carboxyl***
Strain **KoFox** - 3	8.70 ± 0.11	5.15 ± 0.13	Amine

Footnote: *Functional group assignments derived from FTIR spectra analysis of the same samples. **pKa and site concentration values represent the average of 4 replicate experiments. ***Needs confirmation by FTIR.

Part 2: DVLO modeling – zeta potential and surface contact angle data summary

	Zeta potential (mV)	**θ - water (°)**	**θ - Glycerol (°)**	**θ - Diiodomethane (°)**
Strain KB01 (water column in Hegler media)	-25.4 ± 3.7	29.3 ± 4.1	53.5 ± 5.0	50.4 ± 2.9
Strain KoFox (water column in Hegler media)	-4.5 ± 2.3	20.8 ± 3.0	33.4 ± 4.7	52.2 ± 3.1
Abiotic Fe(III) oxyhydroxides precipitated with 1.0 mM Si	-30 ± 2	12.6 ± 1.8	18.7 ± 2.7	0 ± 0

Part 3: DVLO modeling – surface tensions components for the three known liquids, photoferrotrophic cells, and abiotic iron minerals (eq.3).

(in mJ m^{-2})	γ^{TOT}	$\boldsymbol{\gamma^{LW}}$	$\boldsymbol{\gamma^{AB}}$	$\boldsymbol{\gamma^{+}}$	$\boldsymbol{\gamma^{-}}$
Water	72.8	21.8	51.0	25.5	25.5
Diiodomethane	50.8	50.8	0.0	0.0	0.0
Glycerol	64.0	34.0	30.0	3.9	57.4
Strain KB01	36.8	34.1	2.7	0.03	62.8
Strain KoFox	53.8	33.1	20.8	2.1	51.6
Abiotic Fe(III) oxyhydroxides precipitated with 1.0 mM Si	64.1	50.8	13.3	1.0	44.3

Part 4: DVLO modeling – surface free energies for cell-cell (eq.4) and cell-Fe(III) oxyhydroxide (eq.5) interactions.

	Cell-Cell			**Cell-Fe(III) oxyhydroxide**		
(in mJ m^{-2})	ΔG_{iwi}	ΔG_{iwi}^{AB}	ΔG_{iwi}^{LW}	ΔG_{iwj}	ΔG_{iwj}^{AB}	ΔG_{iwj}^{LW}
Strain KB01	53.34	56.07	-2.73	33.30	38.91	-5.61
Strain KoFox	28.41	30.75	-2.33	24.07	29.25	-5.19
Abiotic Fe(III) oxyhydroxides precipitated with 1.0 mM Si	14.45	-12.09	26.54			

Table S3. Modern and Archean Fe fluxes.

Part 1: BIF deposition, demonstrating the depletion of the Fe(II) reservoir

	Individual BIF (*5*)	**Global Fe(II) to deposit BIFs**	**High estimate deep ocean Fe(II) (*76*)**	**Approx. L in ocean based on 75% modern continents**	**Global inventory of Fe(II)**	**Years to deplete Fe(II) from oceans**	**Modern hydro. input: on-axis and off-axis (*41*)**	**Years to deplete with modern hydro. input resupply**
Units	mol/m^2y	$Tmol\ yr^{-1}$	mmol/L	L	Tmol	y	$Tmol\ yr^{-1}$	y
Values	45	4.5	1	$1.12x10^{21}$	$1.12x10^{6}$	249,000	2.18	482,000

Part 2: Newly calculated Fe(II) fluxes to the Archean oceans

Time	**Litho-sphere heat loss ratio**	**Hydro. fluid flow: on-axis**	**Hydro. Fe(II) flux: on-axis***	**Hydro. fluid flow: off-axis**	**Hydro. Fe(II) flux: off-axis****	**Total hydro. Fe(II) flux**	**Total Fe(II) flux: hydro. + continental weathering*****
Ga	N/A	$kg\ yr^{-1}$	$Tmol\ yr^{-1}$	$kg\ yr^{-1}$	$Tmol\ yr^{-1}$	$Tmol\ yr^{-1}$	$Tmol\ yr^{-1}$
4.0	10.9	5.5E+14	32.7	1.5E+17	114.5	147.2	160.3
3.5	5.9	3.0E+14	17.7	8.3E+16	62.0	79.7	89.1
3.0	3.9	2.0E+14	11.7	5.5E+16	41.0	52.7	60.6
2.5	2.8	1.4E+14	8.4	3.9E+16	29.4	37.8	44.9
2.0	2.2	1.1E+14	6.6	3.1E+16	23.1	29.7	36.4
1.5	1.7	8.5E+13	0.51	2.4E+16	17.9	18.4	24.6
1.0	1.4	7.0E+13	0.42	2.0E+16	14.7	15.1	21.2
0.5	1.2	6.0E+13	0.36	1.7E+16	12.6	13.0	18.9
0.0	1.0	5.0E+13	0.30	1.4E+16	10.5	10.8	16.6

Footnote: *On-axis [Fe(II)]: 0-1.5 Ga 6 mmol/kg, 2-4 Ga 60 mmol/kg; **Off-axis [Fe(II)]: 0-4 Ga 0.75 mmol/kg; ***Continental weathering Fe(II) flux: 0-1.5 Ga 0 $Tmol\ yr^{-1}$, 2-4 Ga 5 $Tmol\ yr^{-1}$.

Table S4. Different scenarios of the physical separation model, with each case using a different water velocity.

	Horizontal water velocity*	Distance to deposit 50% of the Fe(III) oxyhydroxides**	Distance to deposit 90% of the Fe(III) oxyhydroxides
Units	m yr^{-1}	km	km
Case 1	**31536**	**1.2**	**13.4**
Case 2	72533	2.7	30.9
Case 3	113530	4.2	48.3
Case 4	154526	5.8	65.7
Case 5	**195523**	**7.3**	**83.2**
Case 6	236520	8.8	100.6
Case 7	277517	10.4	118.1
Case 8	**318514**	**11.9**	**135.5**

Footnote: *Water velocity based on modern ocean current velocities (*52*, *55*); **Density of iron for this calculation was 3.8g mL^{-1}; [3]An upwelling rate of 375m y^{-1} and deep water [Fe] of 37µM were used to calculate the iron deposition rates; [4]Density of carbon for this calculation was 1.075g mL^{-1}. Bold and underlined cases are shown in fig. S6.

Table S5. Data compilations for Fig. 1 and fig. S1.

Part 1: Data for Figure 1 of main text

Banded Iron formation location	% Weight OM	Reference	Deposit Age (Ga)
Fe-rich carbonates (Transvaal supergroup, RSA) 1	0.041	Klein and Buekes, 1989 (*25*)	2.3
Fe-rich carbonates (Transvaal supergroup, RSA) 2	0.36	"	2.3
Siderite-rich BIFs and chert (Transvaal supergroup, RSA)1	0.052	"	2.3
Siderite-rich BIFs and chert (Transvaal supergroup, RSA)2	0.047	"	2.3
Siderite-rich BIFs and chert (Transvaal supergroup, RSA)3	0.11	"	2.3
Siderite-rich BIFs and chert (Transvaal supergroup, RSA)4	0.06	"	2.3
Siderite-rich BIFs and chert (Transvaal supergroup, RSA)5	0.06	"	2.3
Siderite-rich BIFs and chert (Transvaal supergroup, RSA)6	0.144	"	2.3
Siderite-rich BIFs and chert (Transvaal supergroup, RSA)7	0.065	"	2.3
Siderite-rich BIFs and chert (Transvaal supergroup, RSA)8	0.101	"	2.3
Siderite-rich BIFs and chert (Transvaal supergroup, RSA)9	0.041	"	2.3
Siderite-rich BIFs and chert (Transvaal supergroup, RSA)10	0.084	"	2.3
Siderite-rich BIFs and chert (Transvaal supergroup, RSA)11	0.062	"	2.3
Siderite-rich BIFs and chert (Transvaal supergroup, RSA)12	0.203	"	2.3
Siderite-rich BIFs and chert (Transvaal supergroup, RSA)13	0.062	"	2.3

Siderite-rich BIFs and chert (Transvaal supergroup, RSA)14	0.059	"	2.3
Siderite-rich BIFs and chert (Transvaal supergroup, RSA)15	0.065	"	2.3
Siderite-rich BIFs and chert (Transvaal supergroup, RSA)16	0.061	"	2.3
Siderite-rich BIFs and chert (Transvaal supergroup, RSA)17	0.673	"	2.3
Siderite-rich BIFs and chert (Transvaal supergroup, RSA)18	0.104	"	2.3
Siderite-rich BIFs and chert (Transvaal supergroup, RSA)19	0.146	"	2.3
Magnetite-rich, oxide Ifs (Transvaal supergroup, RSA) 1	0.01	"	2.3
Magnetite-rich, oxide Ifs (Transvaal supergroup, RSA) 2	0.017	"	2.3
Magnetite-rich, oxide Ifs (Transvaal supergroup, RSA) 3	0.008	"	2.3
Magnetite-rich, oxide Ifs (Transvaal supergroup, RSA) 4	0.015	"	2.3
Magnetite-rich, oxide Ifs (Transvaal supergroup, RSA) 5	0.013	"	2.3
Magnetite-rich, oxide Ifs (Transvaal supergroup, RSA) 6	0.015	"	2.3
Magnetite-rich, oxide Ifs (Transvaal supergroup, RSA) 7	0.008	"	2.3
Magnetite-rich, oxide Ifs (Transvaal supergroup, RSA) 8	0.008	"	2.3
Magnetite-rich, oxide Ifs (Transvaal supergroup, RSA) 9	0.013	"	2.3
Magnetite-rich, oxide Ifs (Transvaal supergroup, RSA) 10	0.015	"	2.3
Transition zone Kuruman & Griquatown (Transvaal supergroup, RSA) 1	0.017	Beukes and Klein 1990 (*87*)	2.4
Transition zone Kuruman & Griquatown (Transvaal supergroup, RSA) 2	0.019	"	2.4
Transition zone Kuruman & Griquatown (Transvaal supergroup, RSA) 3	0.012	"	2.4
Transition zone Kuruman & Griquatown (Transvaal supergroup, RSA) 4	0.017	"	2.4
Transition zone Kuruman & Griquatown (Transvaal supergroup, RSA) 5	0.015	"	2.4
Transition zone Kuruman & Griquatown (Transvaal supergroup, RSA) 6	0.016	"	2.4
Transition zone Kuruman & Griquatown (Transvaal supergroup, RSA) 7	0.017	"	2.4
Transition zone Kuruman & Griquatown (Transvaal supergroup, RSA) 8	0.018	"	2.4
Transition zone Kuruman & Griquatown (Transvaal supergroup, RSA) 9	0.019	"	2.4
Transition zone Kuruman & Griquatown (Transvaal supergroup, RSA) 10	0.011	"	2.4
Transition zone Kuruman & Griquatown (Transvaal supergroup, RSA) 11	0.016	"	2.4
Transition zone Kuruman & Griquatown (Transvaal supergroup, RSA) 12	0.017	"	2.4
Transition zone Kuruman & Griquatown (Transvaal supergroup, RSA) 13	0.034	"	2.4

Transition zone Kuruman & Griquatown (Transvaal supergroup, RSA) 14	0.012	"	2.4
Transition zone Kuruman & Griquatown (Transvaal supergroup, RSA) 15	0.016	"	2.4
Transition zone Kuruman & Griquatown (Transvaal supergroup, RSA) 16	0.015	"	2.4
Transition zone Kuruman & Griquatown (Transvaal supergroup, RSA) 17	0.022	"	2.4
Transition zone Kuruman & Griquatown (Transvaal supergroup, RSA) 18	0.022	"	2.4
Transition zone Kuruman & Griquatown (Transvaal supergroup, RSA) 19	0.017	"	2.4
Transition zone Kuruman & Griquatown (Transvaal supergroup, RSA) 20	0.024	"	2.4
Transition zone Kuruman & Griquatown (Transvaal supergroup, RSA) 21	0.02	"	2.4
Transition zone Kuruman & Griquatown (Transvaal supergroup, RSA) 22	0.018	"	2.4
Transition zone Kuruman & Griquatown (Transvaal supergroup, RSA) 23	0.02	"	2.4
Transition zone Kuruman & Griquatown (Transvaal supergroup, RSA) 24	0.014	"	2.4
Transition zone Kuruman & Griquatown (Transvaal supergroup, RSA) 25	0.043	"	2.4
Transition zone Kuruman & Griquatown (Transvaal supergroup, RSA) 26	0.025	"	2.4
Transition zone Kuruman & Griquatown (Transvaal supergroup, RSA) 27	0.015	"	2.4
Transition zone Kuruman & Griquatown (Transvaal supergroup, RSA) 28	0.039	"	2.4
Transition zone Kuruman & Griquatown (Transvaal supergroup, RSA) 29	0.03	"	2.4
Transition zone Kuruman & Griquatown (Transvaal supergroup, RSA) 30	0.022	"	2.4
Transition zone Kuruman & Griquatown (Transvaal supergroup, RSA) 31	0.012	"	2.4
Transition zone Kuruman & Griquatown (Transvaal supergroup, RSA) 32	0.015	"	2.4
Transition zone Kuruman & Griquatown (Transvaal supergroup, RSA) 33	0.015	"	2.4
Transition zone Kuruman & Griquatown (Transvaal supergroup, RSA) 34	0.018	"	2.4
Quartz-rich Dales Gorge Member BIF (Dales Gorge, AUS) 1	0.067	Kaufman *et. al.* 1990 (*24*)	2.5
Quartz-rich Dales Gorge Member BIF (Dales Gorge, AUS) 2	0.032	"	2.5
Quartz-rich Dales Gorge Member BIF (Dales Gorge, AUS) 3	0.08	"	2.5
Quartz-rich Dales Gorge Member BIF (Dales Gorge, AUS) 4	0.082	"	2.5
Quartz-rich Dales Gorge Member BIF (Dales Gorge, AUS) 5	0.108	"	2.5
Marra Mamba IF (Pilbara/Hammersley, AUS) 1	0.3	Baur *et. al.* 1985 (*88*)	2.5
Marra Mamba IF (Pilbara/Hammersley, AUS) 2	0.2	"	2.5
Marra Mamba IF (Pilbara/Hammersley, AUS) 3	0.4	"	2.5
Macroband BIF 4 (Dales Gorge Member, AUS) 1	0.3	"	2.5
Macroband BIF 4 (Dales Gorge Member, AUS) 2	0.2	"	2.5
Macroband BIF 4 (Dales Gorge Member, AUS) 3	0.4	"	2.5

Macroband BIF 4 (Dales Gorge Member, AUS) 4	2.6	"	2.5
Macroband BIF 4 (Dales Gorge Member, AUS) 5	2.1	"	2.5
Macroband BIF 4 (Dales Gorge Member, AUS) 6	3.1	"	2.5
Siliceous manganese formations (Urucum, BRA) 1	0.05	Klein and Laderia 2004 (*89*)	0.75
Siliceous manganese formations (Urucum, BRA) 2	0.06	"	0.75
Siliceous manganese formations (Urucum, BRA) 3	0.06	"	0.75
Siliceous manganese formations (Urucum, BRA) 4	0.08	"	0.75
Siliceous manganese formations (Urucum, BRA) 5	0.04	"	0.75
Siliceous manganese formations (Urucum, BRA) 6	0.07	"	0.75
Siliceous manganese formations (Urucum, BRA) 7	0	"	0.75
Siliceous manganese formations (Urucum, BRA) 8	0.06	"	0.75
Quartz-magnetite IF (Isua, GRN) 1	0.06	Dymek and Klein 1988 (*90*)	3.8
Quartz-magnetite IF (Isua, GRN) 2	0.05	"	3.8
Quartz-magnetite IF (Isua, GRN) 3	0.01	"	3.8
Quartz-magnetite IF (Isua, GRN) 4	0.02	"	3.8
Quartz-magnetite IF (Isua, GRN) 5	0.02	"	3.8
Quartz-magnetite IF (Isua, GRN) 6	0.01	"	3.8
Magnesian IF (Isua, GRN) 1	0.11	"	3.8
Magnesian IF (Isua, GRN) 2	0.06	"	3.8
Magnesian IF (Isua, GRN) 3	0.05	"	3.8
Magnesian IF (Isua, GRN) 4	0.03	"	3.8
Aluminous IF (Isua, GRN) 1	0.16	"	3.8
Aluminous IF (Isua, GRN) 2	0.01	"	3.8
Graphitic IF (Isua, GRN) 1	2.98	"	3.8
Graphitic IF (Isua, GRN) 2	1.54	"	3.8
Graphitic IF (Isua, GRN) 3	0.7	"	3.8
Graphitic IF (Isua, GRN) 4	2.09	"	3.8
Carbonate-rich IF (Isua, GRN) 1	1.92	"	3.8
Carbonate-rich IF (Isua, GRN) 2	1.38	"	3.8
Carbonate-rich IF (Isua, GRN) 3	0.27	"	3.8
Carbonate-rich IF (Isua, GRN) 4	1.17	"	3.8
Carbonate-rich IF (Isua, GRN) 5	1.44	"	3.8
Carbonate-rich IF (Isua, GRN) 6	2.13	"	3.8
Carbonate-rich IF (Isua, GRN) 7	1.35	"	3.8
Hematite bearing IF (Riptan, CAN) 1	0.165	Klein and Beukes 1993 (*91*)	0.75
Hematite bearing IF (Riptan, CAN) 2	0.131	"	0.75
Hematite bearing IF (Riptan, CAN) 3	0.147	"	0.75
Proterozoic Minas Supergroup, BIF, Aguas Claras, Carb rich (SE Brazil) 1	0.023	Klein and Laderia 2000 (*92*)	2.5
Proterozoic Minas Supergroup, BIF, Aguas Claras, Carb rich (SE Brazil) 2	0.019	"	2.5
Proterozoic Minas Supergroup, BIF, Aguas Claras, Carb rich (SE Brazil) 3	0.019	"	2.5
Proterozoic Minas Supergroup, BIF, Mutuca (SE Brazil) 1	0.023	"	2.5
Proterozoic Minas Supergroup, BIF, Mutuca (SE Brazil) 2	0.027	"	2.5

Proterozoic Minas Supergroup, BIF, Mutuca (SE Brazil) 3	0.509	"	2.5
Ancient sediments and non-IF rocks			
Shales averages through time 1	0.6	Holland and Schidlowski 1984 p. 103 (*93*)	3.4
Shales averages through time 2	0.85	"	2.7
Shales averages through time 3	1.5	"	2.1
Shales averages through time 4	0.3	"	1.9
Shales averages through time 5	0.4	"	1.1
Shales averages through time 6	0.67	"	0.5
Sediments averages through time 1	0.6	"	3.8
Sediments averages through time 2	0.5	"	3.4
Sediments averages through time 3	1.3	"	2.5
Sediments averages through time 4	0.2	"	2.1
Sediments averages through time 5	0.15	"	1.1
Sediments averages through time 6	0.4	"	0.5
Black Shale, Carajas, overlying BIF (Brazil) 1	1.58	Cabral *et. al*. 2013 (*94*)	2.7
Black Shale, Carajas, overlying BIF (Brazil) 2	1.64	"	2.7
Black Shale, Carajas, overlying BIF (Brazil) 3	0.85	"	2.7
Black Shale, Carajas, overlying BIF (Brazil) 4	2.69	"	2.7
Black Shale, Carajas, overlying BIF (Brazil) 5	2.56	"	2.7
Black Shale, Carajas, overlying BIF (Brazil) 6	3.21	"	2.7
Black Shale, Carajas, overlying BIF (Brazil) 7	2.59	"	2.7
Black Shale, Carajas, overlying BIF (Brazil) 8	3.27	"	2.7
Black Shale, Carajas, overlying BIF (Brazil) 9	2.36	"	2.7
Black Shale, Carajas, overlying BIF (Brazil) 10	1.14	"	2.7
Black Shale, Carajas, overlying BIF (Brazil) 11	1.2	"	2.7
Black Shale, Carajas, overlying BIF (Brazil) 12	0.98	"	2.7
Black Shale, Carajas, overlying BIF (Brazil) 13	1.26	"	2.7
Black Shale, Carajas, overlying BIF (Brazil) 14	1.27	"	2.7
Black Shale, Carajas, overlying BIF (Brazil) 15	1.11	"	2.7
Black Shale, Carajas, overlying BIF (Brazil) 16	1.27	"	2.7
Silverton, Kaapvaal shales, underestimate due to metamosphsis (RSA)	0.9	Watanabe *et. al*., 1997 (*95*)	2.2
Timeball Hill, Kaapvaal shales, underestimate due to metamosphsis (RSA) 1	0.94	"	2.2
Timeball Hill, Kaapvaal shales, underestimate due to metamosphsis (RSA) 2	1.22	"	2.2
Timeball Hill, Kaapvaal shales, underestimate due to metamosphsis (RSA) 3	1.07	"	2.2
Timeball Hill, Kaapvaal shales, underestimate due to metamosphsis (RSA) 4	0.81	"	2.2
Black Reef, Kaapvaal shales, underestimate due to metamosphsis (RSA) 1	1.56	"	2.6
Black Reef, Kaapvaal shales, underestimate due to metamosphsis (RSA) 2	1.72	"	2.6
Black Reef, Kaapvaal shales, underestimate due to metamosphsis (RSA) 3	1.33	"	2.6
Black Reef, Kaapvaal shales, underestimate due to metamosphsis (RSA) 4	1.69	"	2.6
Selati, Kaapvaal shales, underestimate due to metamosphsis (RSA)	0.2	"	2.6

K-8, Kaapvaal shales, underestimate due to metamosphsis (RSA) 1	0.21	"	2.8
K-8, Kaapvaal shales, underestimate due to metamosphsis (RSA) 2	0.23	"	2.8
Carbonaceous shale, Wilpena Group, (South Australia)	1.51	McKirdy 1974 (*96*)	0.65
Shale, Pertatataka Formation (Nothern Territory Australia)	0.89	"	0.7
Shale, Bitter Springs Formation (NT Australia)	0.66	"	0.85
Upper Shale member, Nonesuch shale (Michigan, USA)	0.4	"	1.1
Shale, Muhos Formation, Jotnian Series (Finland)	0.41	"	1.3
Calcereous shale, McMinn Formation, Roper Group (NT Australia)	1.04	"	1.4
HYC Pyritic shale, McArthur Group (NT Australia)	1.85	"	1.6
Carbonaceous , dolomite shale, Gooparla Group (NT Australia)	2.25	"	1.9
Carbonaceous shale, Soudan Iron Formation (Minnesota, USA)	3.2	"	2.7
Hematite mudstone (Rapitan IF, surrounding lithologies) 1	0.128	Klein and Beukes 1993 (*91*)	0.75
Hematite mudstone (Rapitan IF, surrounding lithologies) 2	0.134	"	0.75
Volcaniclastic mudstone (Rapitan IF, surrounding lithologies) 1	0.189	"	0.75
Shale (Rapitan IF, surrounds lithologies) 1	0.23	"	0.75
Shale (Rapitan IF, surrounds lithologies) 2	0.261	"	0.75
Shale (Rapitan IF, surrounds lithologies) 3	0.522	"	0.75
Shale (Transvaal supergroup, RSA) 1	5.33	Klein and Beukes 1989 (*25*)	2.3
Shale (Transvaal supergroup, RSA) 2	3.77	"	2.3
Shale (Transvaal supergroup, RSA) 3	2.62	"	2.3
Shale (Transvaal supergroup, RSA) 4	2.73	"	2.3
Shale (Transvaal supergroup, RSA) 5	4.95	"	2.3
Shale (Transvaal supergroup, RSA) 6	6.36	"	2.3
Shale (Transvaal supergroup, RSA) 7	3.84	"	2.3
Shale (Transvaal supergroup, RSA) 8	4.19	"	2.3
Shale (Transvaal supergroup, RSA) 9	2.79	"	2.3
Shale (Transvaal supergroup, RSA) 10	2.52	"	2.3
Modern environments			
Molenplaat, Schelde estuary, intertidal (Netherlands) 1	0.309	Middelburg *et. al*. 1999 (*97*)	
Molenplaat, Schelde estuary, intertidal (Netherlands) 2	0.372	"	
Molenplaat, Schelde estuary, intertidal (Netherlands) 3	0.158	"	
Molenplaat, Schelde estuary, intertidal (Netherlands) 4	0.093	"	
Molenplaat, Schelde estuary, intertidal (Netherlands) 5	0.108	"	
Iberian Margin, 175m-4909m depth (Atlantic Ocean) 1	0.407	"	
Iberian Margin, 175m-4909m depth (Atlantic Ocean) 2	0.24	"	

Iberian Margin, 175m-4909m depth (Atlantic Ocean) 3	0.22	"	
Iberian Margin, 175m-4909m depth (Atlantic Ocean) 4	0.63	"	
Iberian Margin, 175m-4909m depth (Atlantic Ocean) 5	0.51	"	
13m-1997m (Northwestern Black Sea) 1	1.262	"	
13m-1997m (Northwestern Black Sea) 2	0.783	"	
13m-1997m (Northwestern Black Sea) 3	1.638	"	
13m-1997m (Northwestern Black Sea) 4	2.147	"	
13m-1997m (Northwestern Black Sea) 5	1.111	"	
13m-1997m (Northwestern Black Sea) 6	2.997	"	
13m-1997m (Northwestern Black Sea) 7	4.459	"	
13m-1997m (Northwestern Black Sea) 8	5.26	"	
13m-1997m (Northwestern Black Sea) 9	2.288	"	
2.7m-270m (North Sea) 1	2.093	"	
2.7m-270m (North Sea) 2	2.424	"	
2.7m-270m (North Sea) 3	0.559	"	
2.7m-270m (North Sea) 4	0.078	"	
2.7m-270m (North Sea) 5	0.219	"	
2.7m-270m (North Sea) 6	0.055	"	
5400m (Madeira Abyssal Plain) 1	0.182	"	
5400m (Madeira Abyssal Plain) 2	0.228	"	
5400m (Madeira Abyssal Plain) 3	0.361	"	
5400m (Madeira Abyssal Plain) 4	1.139	"	
5400m (Madeira Abyssal Plain) 5	1.137	"	
2539m (Eastern Mediterranean) 1	0.417	"	
2539m (Eastern Mediterranean) 2	0.222	"	
2539m (Eastern Mediterranean) 3	2.598	"	
Western continental slope India OMZ, 85m-2297m (Arabian Sea) 1	0.14	Paropkari *et. al.* 1993 (*98*)	
Western continental slope India OMZ, 85m-2297m (Arabian Sea) 2	1.1	"	
Western continental slope India OMZ, 85m-2297m (Arabian Sea) 3	2.81	"	
Western continental slope India OMZ, 85m-2297m (Arabian Sea) 4	2.07	"	
Western continental slope India OMZ, 85m-2297m (Arabian Sea) 5	2.51	"	
Western continental slope India OMZ, 85m-2297m (Arabian Sea) 6	0.57	"	
Western continental slope India OMZ, 85m-2297m (Arabian Sea) 7	3.4	"	
Western continental slope India OMZ, 85m-2297m (Arabian Sea) 8	4.14	"	
Western continental slope India OMZ, 85m-2297m (Arabian Sea) 9	0.79	"	
Western continental slope India OMZ, 85m-2297m (Arabian Sea) 10	5.88	"	
Western continental slope India OMZ, 85m-2297m (Arabian Sea) 11	3.33	"	
Western continental slope India OMZ, 85m-2297m (Arabian Sea) 12	2.76	"	

Western continental slope India OMZ, 85m-2297m (Arabian Sea) 13	5.06	"	
Western continental slope India OMZ, 85m-2297m (Arabian Sea) 14	5.47	"	
Western continental slope India OMZ, 85m-2297m (Arabian Sea) 15	6.18	"	
Western continental slope India OMZ, 85m-2297m (Arabian Sea) 16	2.33	"	
Western continental slope India OMZ, 85m-2297m (Arabian Sea) 17	1.9	"	
Western continental slope India OMZ, 85m-2297m (Arabian Sea) 18	2.07	"	
Western continental slope India OMZ, 85m-2297m (Arabian Sea) 19	3.21	"	
Western continental slope India OMZ, 85m-2297m (Arabian Sea) 20	1.35	"	
Western continental slope India OMZ, 85m-2297m (Arabian Sea) 21	0.98	"	
Western continental slope India OMZ, 85m-2297m (Arabian Sea) 22	0.66	"	
Western continental slope India OMZ, 85m-2297m (Arabian Sea) 23	0.79	"	
Western continental slope India OMZ, 85m-2297m (Arabian Sea) 25	0.59	"	
Western continental slope India OMZ, 85m-2297m (Arabian Sea) 25	0.69	"	
Chilean continental slope OMZ (Pacific Ocean) 1	5	Niggemann *et. al*. 2007 (*99*)	
Chilean continental slope OMZ (Pacific Ocean) 2	5.25	"	
Chilean continental slope OMZ (Pacific Ocean) 3	6	"	
Chilean continental slope OMZ (Pacific Ocean) 4	5.5	"	
Chilean continental slope OMZ (Pacific Ocean) 5	5.5	"	
Chilean continental slope OMZ (Pacific Ocean) 6	6	"	
Chilean continental slope OMZ (Pacific Ocean) 7	2	"	
Chilean continental slope OMZ (Pacific Ocean) 8	1.9	"	
Chilean continental slope OMZ (Pacific Ocean) 9	1.8	"	
Chilean continental slope OMZ (Pacific Ocean) 10	3.4	"	
Chilean continental slope OMZ (Pacific Ocean) 11	3.7	"	
Chilean continental slope OMZ (Pacific Ocean) 12	4.4	"	
Chilean continental slope OMZ (Pacific Ocean) 13	4.1	"	
Chilean continental slope OMZ (Pacific Ocean) 14	4.1	"	
Chilean continental slope OMZ (Pacific Ocean) 15	4.1	"	
Chilean continental slope OMZ (Pacific Ocean) 16	2.9	"	
Chilean continental slope OMZ (Pacific Ocean) 17	3	"	
Chilean continental slope OMZ (Pacific Ocean) 18	3	"	
Chilean continental slope OMZ (Pacific Ocean) 19	2.1	"	
Chilean continental slope OMZ (Pacific Ocean) 20	2.1	"	
Chilean continental slope OMZ (Pacific Ocean) 21	2	"	
Chilean continental slope OMZ (Pacific Ocean) 22	2.6	"	
Chilean continental slope OMZ (Pacific Ocean) 23	2.5	"	
Chilean continental slope OMZ (Pacific Ocean) 24	2.5	"	

Part 2: Data for SI Figure 1

Age (Ga)	Iron redox state	BIF type	Reference	% Fe_2O_3	% FeO
3.8	2.56	Isua QM IF	Dymek and Klein 1988 (*90*)	18.17	13.03
3.8	2.16	Isua Al IF	"	4.98	23.5
3.8	2.30	Isua G IF	"	11.98	24.65
3.8	2.08	Isua C IF	"	1.87	18.19
2.7	2.96	Carajas BIF	Klein and Ladeira 2002 (*100*)	58.95	1.97
2.5	2.48	Dales Gorge	Kaufman et al 1990 (*24*)	12.91	13.97
2.5	2.97	Minas BIF	Klein and Ladeira 2000 (*92*)	36.61	1.17
2.4	2.29	RSA Ste IF	Beukes and Klein 1990 (*87*)	9.16	19.8
2.4	2.49	RSA K IF	"	17.42	16.16
2.4	2.48	RSA G IF	"	17.72	17.29
2.3	2.05	RSA Sid IF	Klein and Beukes 1989 (*25*)	1.196	22.58
2.3	2.54	RSA Ox IF	"	22.72	17.56
2	2.43	Labrador BIF	Klein 1966 (*101*)	9.23	11.2
0.75	2.98	Rapitan whole BIF	Klein and Beukes 1993 (*91*)	43.78	0.69
0.75	2.97	Urucum BIF	Klein and Ladeira 2004 (*89*)	37.73	1.08

Supplementary Figures

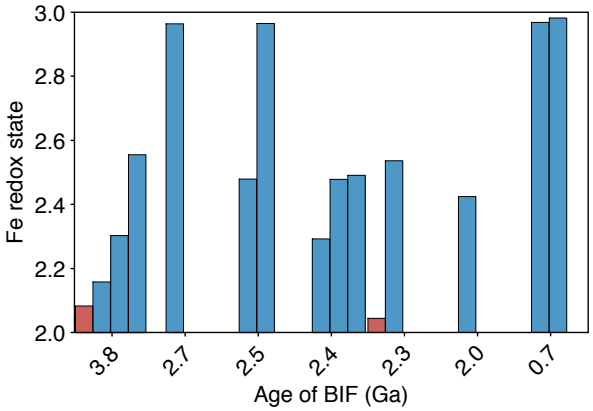

Fig. S1. The redox state of iron in BIF through time where the red bars indicate the siderite-rich BIFs. The overall average redox state of BIFs is 2.4, whereas the average redox state of Archean Eon BIFs, excluding the anomalous siderite rich units is 2.6. References for this figure can be found in Table S5.

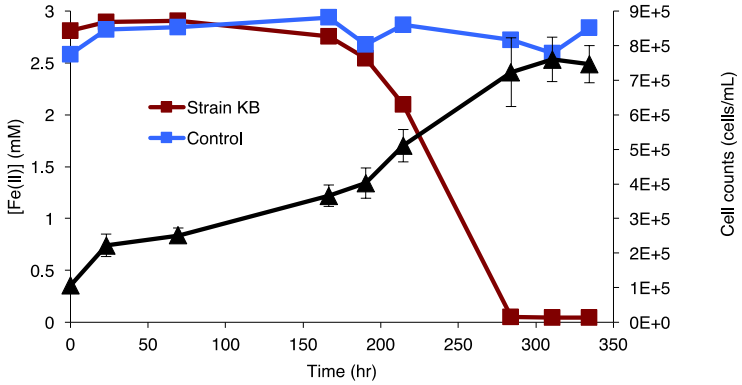

Fig. S2. Growth curve for *C. phaeoferrooxidans* strain KB01. Fe(II) oxidation by *Chlorobium phaeoferrooxidans* strain KB01 (red squares) compared to a non-inoculated control (blue squares) on the left vertical axis. On the right vertical axis, cell counts in cells/mL for the strain KB01 bottle are shown in black triangles. Strain KB01 was capable of oxidizing Fe(II) at rates up to 27 µM/hr.

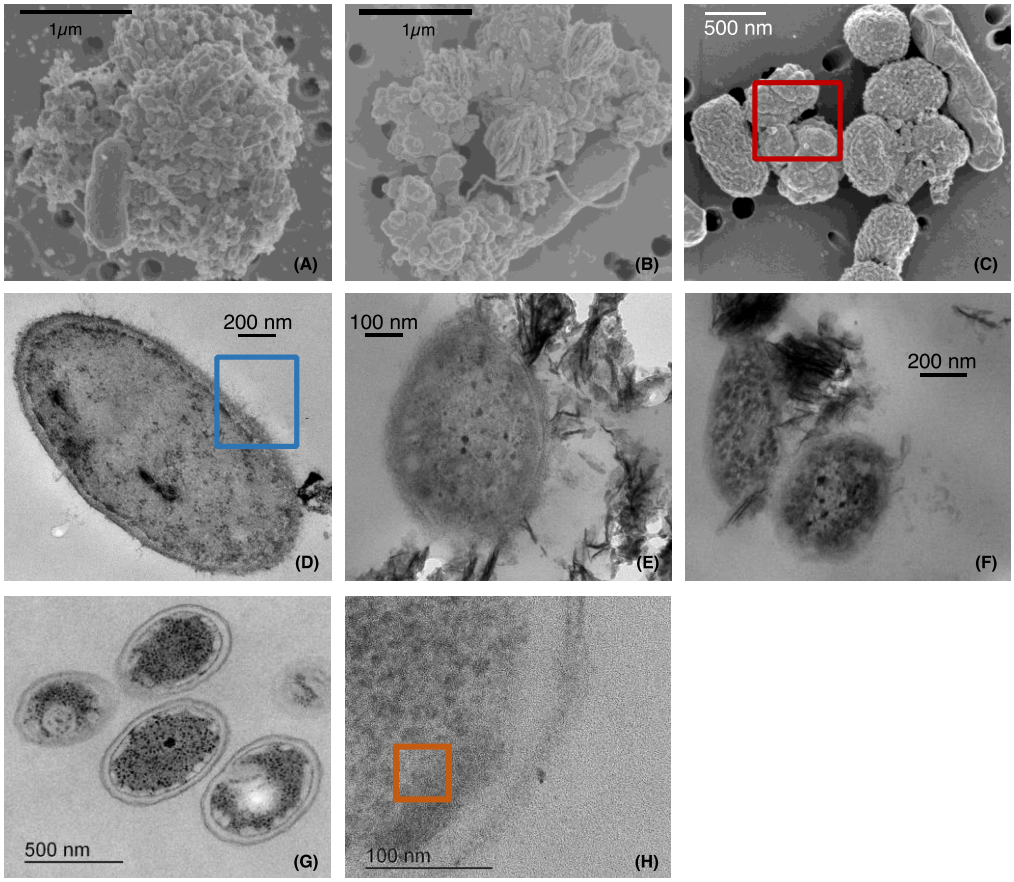

Fig. S3. Additional SEM and TEM images of strains KB01 and KoFox under two conditions. SEM (a,b,c) and TEM (d,e,f,g,h) images showing KoFox cells forming a loose association with Fe(III) particles, but no encrustation (a,b,c). Note the area with the red square in image c denotes iron particles confirmed through EDS spectrum. TEM images (d,e,f) showing KoFox cells forming a loose association with Fe(III) particles. Note the area with the blue square in image d denotes the bacterial capsule. Finally, TEM images (g,h) show multiple KB01 cells without any visible Fe(III) present (g) and a KB01 cell with an Fe(III) nanoparticle noted with the orange square (h).

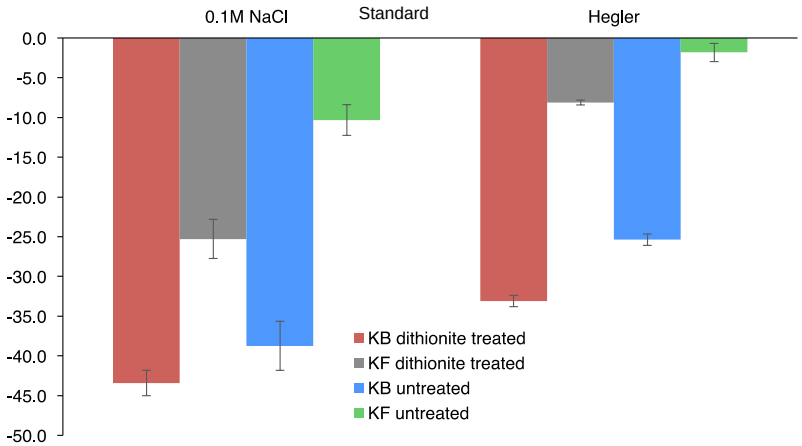

Fig. S4. Surface charge of strains KB01 and KoFox. Zeta potential of strain KB01 and strain KoFox (dithionite treated – red and grey; untreated – blue and green) with two different wash solutions: 0.1M NaCl and Fe free standard media (as described in materials and methods).

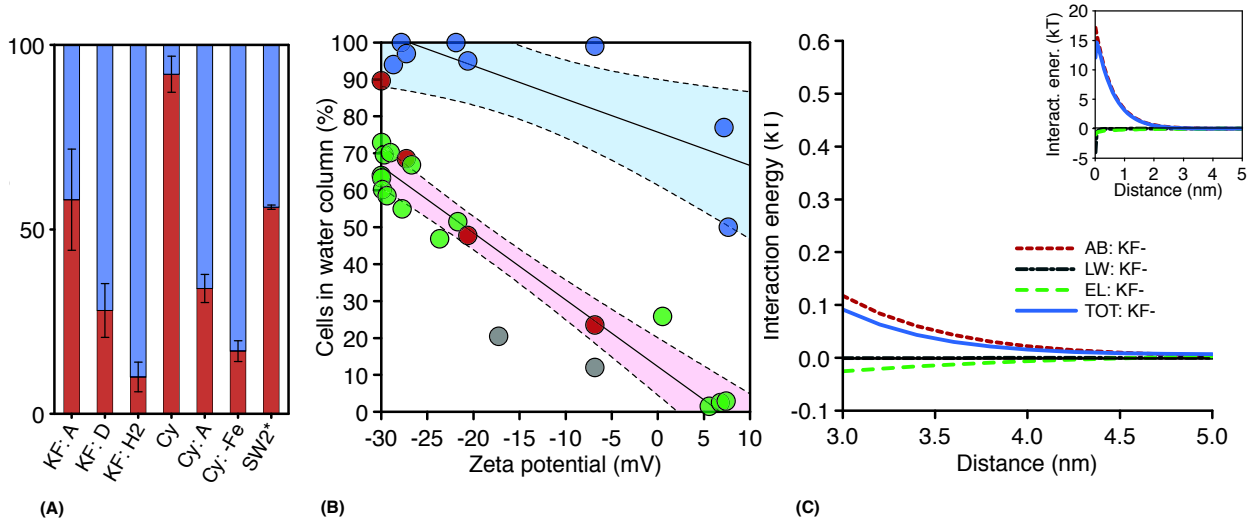

Fig. S5. Additional cell surface characteristics for strain KoFox. The fractions of planktonic (blue) versus sedimented (red) cells (A) for treatments not shown in the main text. The following conditions are represented for the following strains: 400µM Fe, low P (3 µM), with 0.6mM Si [A] for strain KoFox and *Synechococcus*, 10mM Fe, 4.4 mM P [D] and Hydrogen gas with 4.4mM P [H2] for Strain KoFox, 400µM Fe with low P (3 µM) [unmarked] and no Fe with low P (3 µM) [-Fe] for *Synechococcus*, and 0.8-2 mM Fe with 4.4 mM P [*] for strain SW2 (*102*). The relationship between the percentage of cells in the water column and the surface charge of the Fe(III) particles (B) with KoFox (red), Cyanobacteria (green), and SW2 (grey) following a strong downward trend while KB01 (blue) only decreases once Fe(III) particles become positive. The shaded areas represent a 95% confidence interval. Finally, the extended DVLO modeling for strain KoFox (C) with the main graph depicting the interaction energies of the 3 forces and the total for those forces from 3nm-5nm, while the inset depicts the forces from 0nm-5nm. AB refers to the acid-base force, LW the Lifshitz-van der Waals force, EL the electrostatic force, and TOT the total of all three forces.

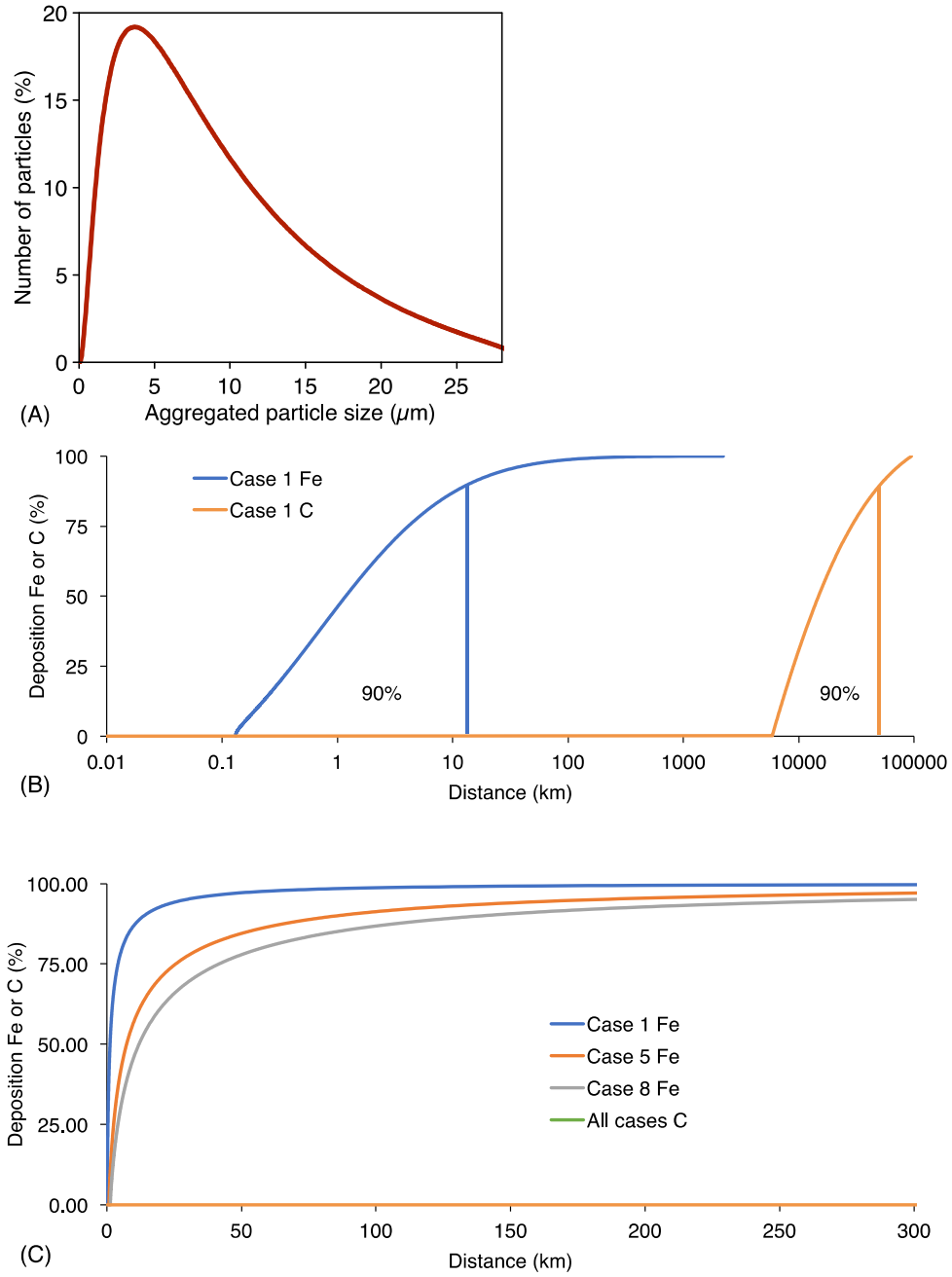

Fig. S6. Modeling the settling velocity of carbon and iron using a range of horizontal current velocities. Percentage of Fe(III) particles (A) that are present at each particle size, in µm, when Fe(III) oxyhydroxides are precipitated abiotically in media with 1.0mM Si and measured using a Mastersizer2000. These data were used to inform the deposition of iron oxyhydroxides in the iron-biomass separation model. The distance over which iron oxyhydroxides (blue curve) and carbon particles (orange curve) deposit for case 1 (B) when an outflow rate of 3.6 m y^{-1} is applied to the particles of iron oxyhydroxides and carbon respectively. The distance that 90% of the Fe(III) oxyhydroxides or carbon travels is denoted under each curve. The distance over which iron oxyhydroxides particles deposit for cases 1, 5, and 8 (C) with the distance that the carbon particles travel not shown in the distance covered by the graph.

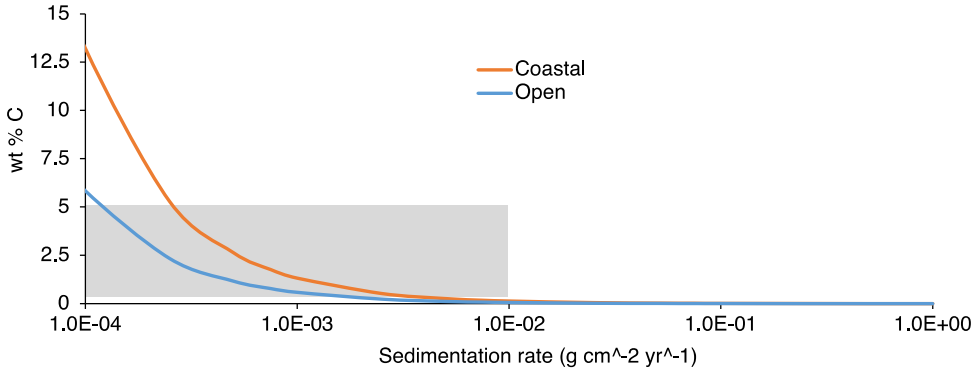

Fig. S7. Modeled weight % organic carbon in the coastal and open ocean sediments. This figure depicts the weight % organic carbon using the values generated in the benchmark model run (2.5 Ga mid, Table 1 – main text). The grey box indicates the range of modern marine sedimentation rates for coastal and open ocean sediments (*103*) on the x-axis and the range of wt% C found in Precambrian shales (Figure 1 – main text; Table S5) on the y-axis.

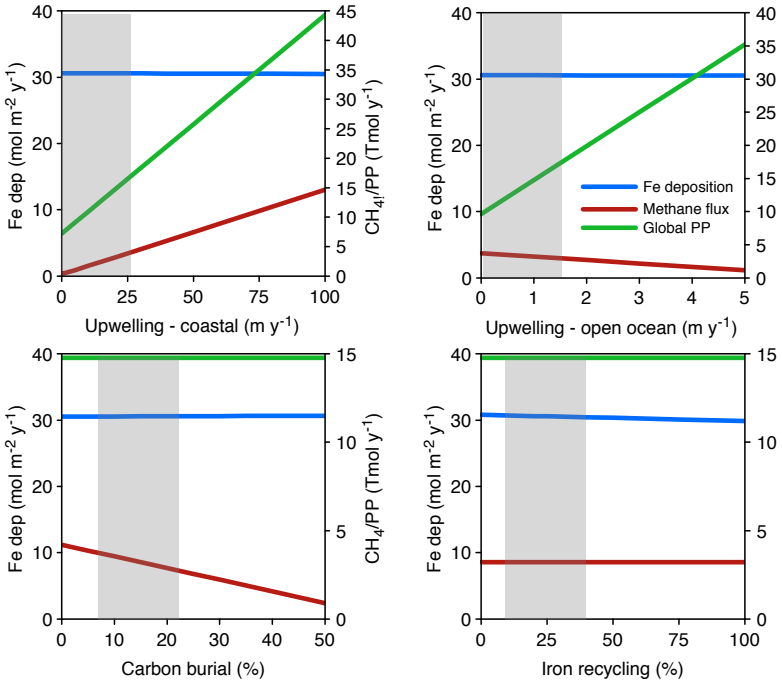

Fig. S8. Iron and carbon box model sensitivity results. Model sensitivity results for varying upwelling rates in the coastal provinces (a), varying upwelling rates in the open ocean provinces (b), varying percentages of carbon burial (c), and varying percentages of iron recycling (d). Iron deposition rates in the upwelling provinces are depicted on the left y-axis, while global rates of primary production and methane production are both shown on the right y-axis in Tmol yr^{-1}.